

Research Highlights

Research Highlights

Introduction

The year 2000 reaches an important milestone for SRRC in terms of the development of VUV and soft X-ray facilities at Taiwan Light Source. At the end of this year, all VUV and soft X-ray ports have been occupied with beamlines. Most of these beamlines are already open for experiments. (See Beamlines Section.) Especially, the new experimental capabilities brought by the three insertion devices U5, U9, and EPU offer new challenging scientific opportunities to our users.

Following the opening of three wiggler beamlines last year for hard X-ray facilities, the X-ray absorption spectroscopy and high-resolution diffraction/scattering are now routinely used for materials studies. Equally exciting is the commissioning of the first Taiwan contract beamline at SPring-8, the bending magnet beamline SP8-12B2, in late 2000. The high energy X-rays of 10 to 70 KeV from this beamline complement greatly to our wiggler source at home.

To promote life science research, specific focus for the last two years has been in the implementation of the protein crystallography station on wiggler 17B beamline. The X-ray protein crystallography capability has been demonstrated by the first unknown structure solved with the data collected at this wiggler station. Current work includes the up-grade of the wiggler station and the construction of a new station at our SPring-8 bending magnet beamline SP8-12B2.

The Research Highlights are grouped into four areas in line with the SRRC's experimental capabilities: gas phase research, materials research on VUV and soft X-ray beamlines, materials research on hard X-ray beamlines, and the development of microstructure fabrication facility.

Research on Gas Phase

Research on the gas phase includes absorption cross section measurements, fluorescence excitation and quenching studies, photoionization and photodissociation studies, and photoelectron - photoion coincidence spectroscopy. These experiments were mainly performed at the Seya-Namioka beamline, but migration to High Flux (03A) and U9 (21A) is expected to take place next year. Results are highlighted in the following.

Planet Atmosphere: Absorption Cross Sections of HCl/DCI and C₂H₆/C₂H₅D (B.-M. Cheng, SRRC; Y.-P. Lee, NTHU)

In light of the new results of Photo-Induced Fractionation Effect (PHIFE) for explaining the gross difference of atmospheric D/H ratios among solar planets, absorption cross sections of hydrogen compounds and their deuterated isotopomers were measured with a double beam absorption cell. The new data on HCl/DCI and C₂H₆/C₂H₅D are used for modeling the atmosphere of Venus and Jupiter, respectively. Preliminary results indicate excellent agreement with the PHIFE mechanism.

CH₃CFCI⁺ Produced from CH₃CFCI₂⁺ (S.-Y. Chiang, SRRC; Y.-P. Lee, NTHU)

Dissociation of energy-selected CH₃CFCI₂ to form CH₃CFCI⁺ has been studied with a molecular beam/threshold photoelectron photoion coincidence system. Thermochemical threshold to form CH₃CFCI⁺ was determined to be 11.10 ± 0.09 V; with this threshold, $I_{H_0}^0(\text{CH}_3\text{CFCI}^+) = 149.0 \pm 2.1$ kcal mol⁻¹ was also derived. Ab initio calculations with G3B3 method were performed for derivation of heats of formation of CH₃CFCI₂, CH₃CFCI, and their

corresponding cations. Based on the experimental and theoretical results, an energy diagram for dissociation of $\text{CH}_3\text{CFCI}_2^+$ into channel of $\text{CH}_3\text{CFCI}^+ + \text{Cl}$ was constructed. (Figure 1)

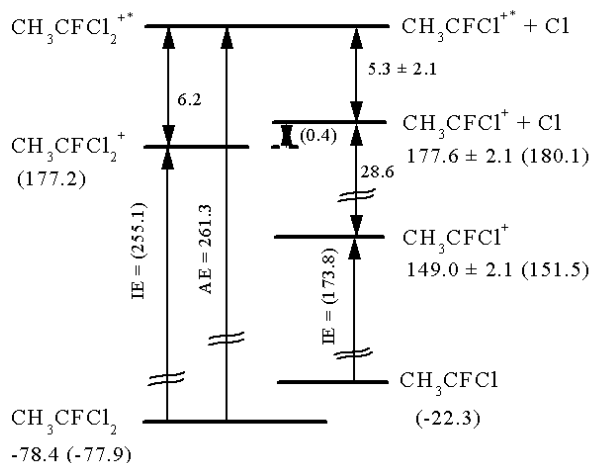


Figure 1 Schematic energy diagram for dissociative photoionization of CH_3CFCI_2 to form $\text{CH}_3\text{CFCI}^+ + \text{Cl}$ based on experimental and calculated results; the values are in kcal mol^{-1} and calculated ΔH_f^0 or IE are listed in parentheses.

Fluorescence Quenching of NO (C. T. Kuo, NSYSU; J. B. Nee, NCU)

NO fluorescence quenched by He, Ar, Xe, N_2 , and CO_2 was investigated in the excitation wavelength region 170 - 230 nm by observing fluorescence in the region 160 - 650 nm. The quenching behavior of fluorescence at C(0) and D(0) is enhanced with increasing He pressure and becomes independent of He pressure around 40 Torr. The enhancement of fluorescence intensity is attributed to the collisional removal of predissociation; a possible mechanism is collision-induced relaxations $\text{C} \rightarrow \text{A}$ and $\text{B} \rightarrow \text{A}$. The quenching half-pressure, rates, and cross sections are obtained and the well depths of NO-rare gas van der Waals molecules are derived based on Parmenter's model.

Photodissociation of CH_3OH in Solid Matrix (B.-M. Cheng, SRRC; Y.-P. Lee, NTHU)

To determine the photodissociation threshold of OH

produced from CH_3OH in solid Ne and Ar at 4 K, the laser-induced fluorescence of OH were monitored while scanning the energy of synchrotron radiation. The thresholds were obtained to be 7.13 ± 0.02 eV in Ne and 7.08 ± 0.04 eV in Ar, respectively; both values are greater than in the gaseous phase value 3.950 eV due to matrix effects.

Condensed Matter Research at VUV and Soft X-ray Beamlines

The highlights of research on condensed matter in the VUV and soft X-ray region are grouped in three areas: (a) photoelectron spectroscopy, (b) soft X-ray absorption spectroscopy, and (c) photoelectron microscopy.

(a) Photoelectron Spectroscopy

Spin-resolved Electronic Structure of Fe_3O_4 (D. J. Huang, SRRC)

Spin-resolved electronic structure of epitaxial Fe_3O_4 films grown in-situ on cleaved $\text{MgO}(100)$ substrates were studied by using spin-resolved photoemission measurements. As shown in Figure 2, the spin-polarization of the top of the valence band has been found to be only -40%. These results are explained in

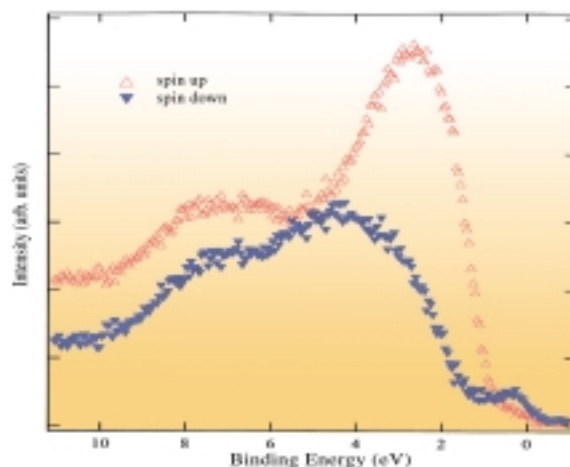


Figure 2 Spin polarized photoemission spectra of $\text{Fe}_3\text{O}_4/\text{MgO}(100)$.

terms of strong-electron correlation effects that set an upper limit for the spin polarization of the first ionization state at about -67%. The conclusion of the experiments does not support the LSDA prediction which expects Fe_3O_4 to be a half-metallic material.

Phosphine Adsorbed on Si(001)-2x1
(D. S. Lin, NCTU)

The surface chemistry of the PH_3 adsorption on Si(001)- 2×1 at elevated temperatures was studied using both core-level photoemission and scanning tunneling microscopy. The PH_2 - PH_3 pairs configuration in the interface at room temperature is immediately washed off at about 550 K, leaving only atomic phosphors to displace one-fourth region of the surface silicon atoms. The decomposed hydrogen covers the other three-fourth region. The displaced silicon diffuses either to the step edge or to nucleate into islands.

Ge Adatoms on Si(001)-2x1
(T.-W. Pi, SRRC)

Ge adatoms on Si(001)- 2×1 was investigated by employing high-resolution photoemission spectrum. The initial stages of the development of a Ge adatom layer on a clean Si(001)- 2×1 surface are consistent with adsorption on random surface sites with limited surface mobility. A critical comparison of the rate of attenuation of core-level signal of the Si buckled dimer up-atoms by Ge deposition, the growth of the two well-resolved features of the Ge adatom spectrum rules out the substitution of Ge into the Si dimers. Instead, Ge atoms are captured by the dangling bonds of the Si dimers, initially as isolated Ge atoms, then as dimers, and finally in clusters.

Ti Silicide Formation on Si(111)-7x7
(A. B. Yang, THU; L. J. Chen, NTHU)

The reaction of Ti atoms with the Si(111)- 7×7 surface was studied with both photoemission and STM techniques. STM showed that Ti atoms favor the adatom sites of the faulted halves of Si surface at initial

deposition. More than four monolayers of Ti are needed to form silicide phase as revealed by Si 2p core-level and valence band photoemission spectra.

Metal Nitrides by CVD
(H. T. Chiu, NCTU; Y. W. Yang, SRRC)

Surface decomposition of CVD precursors for depositing TaN and WN on Cu surface was tracked in this work. Surface reaction and mechanism were proposed to account for the presence of a series of products detected with both photoemission and thermal desorption techniques.

(b) Soft X-ray Absorption Spectroscopy
Metal-Insulator Transition in $\text{Ca}_{2-x}\text{Sr}_x\text{RuO}_4$
(L. H. Tjeng, Univ. of Groningen, The Netherlands)

A quasi-two-dimensional system $\text{Ca}_{2-x}\text{Sr}_x\text{RuO}_4$ shows an interesting evolution from a Mott insulator Ca_2RuO_4 to a triplet superconductor Sr_2RuO_4 . In these

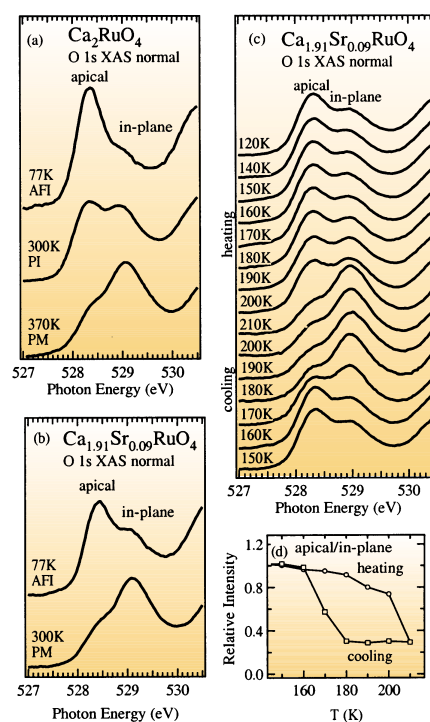


Figure 3 O 1s XAS spectra of Ca_2RuO_4 (a) and $\text{Ca}_{1.91}\text{Sr}_{0.09}\text{RuO}_4$ (b). Hysteresis in the O 1s XAS (c) and the relative intensity of apical component to in-plane one (d).

Ru oxides, four electrons (two holes) occupy the three nearly degenerate 4d t_{2g} orbitals and the orbital degree of freedom is expected to be important. Using O 1s X-ray absorption spectroscopy, we have studied the t_{2g} orbital symmetry in Ca_2RuO_4 and $\text{Ca}_{1.91}\text{Sr}_{0.09}\text{RuO}_4$ and have found a drastic orbital changeover as a function of temperature. (Figure 3)

Size Effect on Superconductivity in $(\text{R}_{0.8}\text{Pr}_{0.2})\text{Ba}_2\text{Cu}_3\text{O}_7$ (J. M. Chen, SRRC)

The depression rate of T_c by Pr doping is R-radius dependence in $(\text{R}_{1-x}\text{Pr}_x)\text{Ba}_2\text{Cu}_3\text{O}_7$ with fixed x. The smaller the atomic number of rare-earth elements in host compounds is, the greater the decrease in T_c is. The variations of electronic structure related to the ionic size of R-site elements in $(\text{R}_{0.8}\text{Pr}_{0.2})\text{Ba}_2\text{Cu}_3\text{O}_7$ for R = Y, Tm, Dy, Gd, Eu, and Sm were investigated by soft X-ray absorption spectroscopy. As deduced from O K-edge X-ray absorption spectra, the hole content from the CuO_2 planes decreases monotonically with increasing ionic size of the R^{3+} ions. It is concluded that the quenching of superconductivity in $(\text{R}_{0.8}\text{Pr}_{0.2})\text{Ba}_2\text{Cu}_3\text{O}_7$ with various ionic radius of R-site elements results predominantly from the hole depletion.

Electronic Structure of I_2 , HgI_2 and HgBr_2 Intercalated BSCCO (2212) (K. B. Garg, Univ. of Rajasthan, India)

Intercalation of molecules between the adjacent Bi_2O_2 layers in BSCCO (2212) results into lengthening of the c-axis (3.6 Å for I_2 and 7.2 Å for HgBr_2 and HgI_2), which may consequently lead to weakening of the coupling between the CuO_2 layers in the consecutive blocks. Intercalation of I_2 molecule into BSCCO (2212) was found to cause a significant depression in T_c by 13-15 K but for intercalation of much larger HgBr_2 and HgI_2 molecules decrease in T_c was found to be only about 5-7 K. Figure 4 represents the results of our polarized measurements on the O K-edge in the orientation E//ab for the pristine, I_2 , HgI_2

and HgBr_2 intercalated BSCCO (2212) single crystals. Our study shows that it is only in case of I_2 intercalation that the crystal becomes overdoped while in the case of other two, it becomes underdoped.

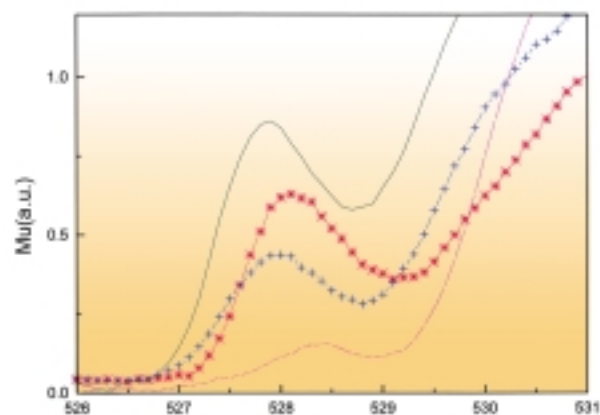


Figure 4 The pre-peak intensities of the O K-edge, E//ab spectra from I_2 [solid line], HgBr_2 [violet dashes at bottom] intercalated and the pristine BSCCO(2212) [red dots and line].

Orbital Character of O 2p States in CrO_2 (D. J. Huang, SRRC)

Orbital character of O 2p states in CrO_2 was investigated for the expected metallic behavior. Polarization-dependent O 1s absorption spectra of epitaxial CrO_2 thin film with two orthogonal light polarization directions have been measured. As shown in Figure 5, the distinct absorption peak at the photon

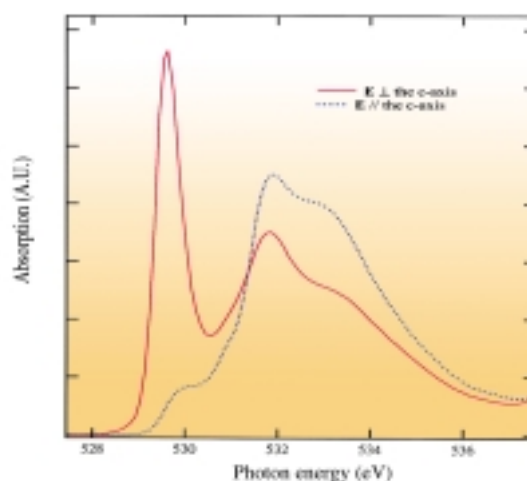


Figure 5 The O 1S absorption spectra of epitaxial CrO_2 thin film with two orthogonal light polarization directions.

energy of 529.6 eV in the absorption spectrum with the light polarization normal to the c-axis is predominately resulted from the hybridized states between O $2p_{x-y}$ and Cr $3d_{xz-yz}$. This absorption peak is strongly reduced when the E vector is parallel to the c-axis, as shown in the dashed line. Their polarization-dependent absorption measurements, therefore, suggest that the states between E_F and 1eV above are strongly dominated by d_{xz-yz} symmetry.

(c) Photoelectron Microscopy

SPEM at U5
(I.-H. Hong, SRRC)

The scanning photoemission microscopy (SPEM) at U5 beamline has achieved a spatial resolution of 0.2 μm . Various test samples have been utilized to demonstrate image quality, spatial and energy resolution, as well as the capability of chemical microanalysis.

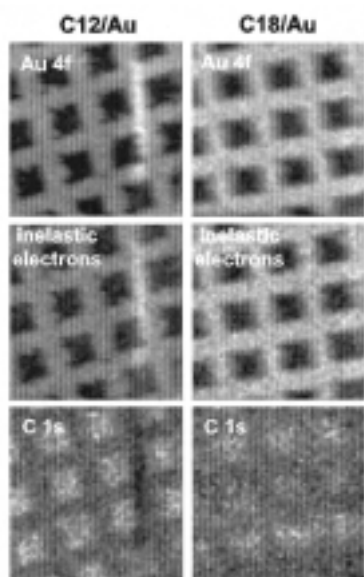


Figure 6 Au 4f, C 1s, and C KLL SPEM images of the C12 and C18 films exposed to 10 eV electrons through a mask. The irradiated areas (squares) reveal a smaller Au 4f intensity and a higher C 1s and C KLL intensity, which is related to the adsorption of the airborne carbon-containing molecules. (image size: $60 \times 60 \mu\text{m}^2$)

Patterned Alkanethiol SAMs
(M. M, Zharnikov, Universitat Heidelberg, Germany; R. Klauser, I.-H. Hong, SRRC)

The alkanethiol self-assembled monolayers (SAMs) on Au have been patterned by low-energy electron irradiation through a mask, which results in a partial damage of the film. The treated and non-treated areas can be clearly distinguished in the SPEM images of Au 4f and C 1s core levels. The adsorption of carbon-containing molecules from ambient onto the irradiated areas gave new insights in the reactivity of the damaged film. Modification of SAMs by electron or X-ray radiation can be used as lithographic approach to pattern surfaces. (Figure 6)

AFM-patterned Si_3N_4 Films
(R. Klauser, I.-H. Hong, SRRC; S. Gwo, NTHU)

It has been recently demonstrated that atomic force microscope (AFM) probe can induce local oxidation to convert thin Si_3N_4 films into SiO_x . With SPEM and MicroXPS techniques, the degree of conversion, i.e., the determination of the x-value depending on AFM tip bias and other preparation parameters could be identified for the first time. This is an important result in understanding the origin and mechanism of Si_3N_4 oxidation by AFM tip. (Figure 7)

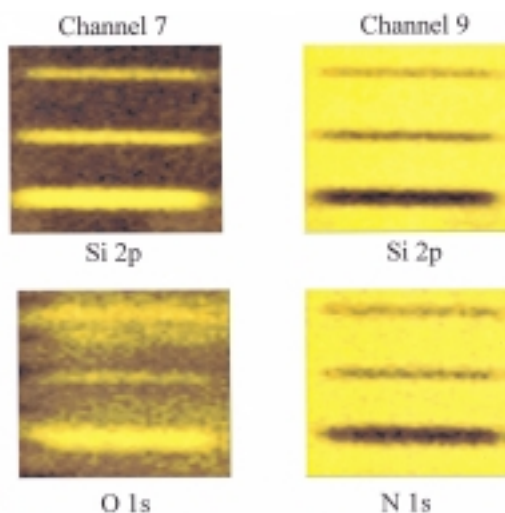


Figure 7 Si 2p, O 1s and N 1s SPEM images of three different SiO_x stripes on Si_3N_4 patterned by AFM. Image size: $24 \times 30 \mu\text{m}^2$, photon energy: 642 eV.

Condensed Matter Research at Hard X-ray Beamlines

The highlights of research on condensed matter in the hard X-ray region are grouped in three areas: (a) hard X-ray absorption spectroscopy, (b) X-ray diffraction/scattering, and (c) protein X-ray crystallography.

(a) Hard X-ray Absorption Spectroscopy

Valence of Ru in the $\text{RuSr}_2\text{GdCu}_2\text{O}_8$ Superconductors (R. S. Liu, NTU)

Ru valence in $\text{RuSr}_2\text{GdCu}_2\text{O}_8$ compounds is important to understand the coexistence of ferromagnetism ($T_M \sim 132\text{K}$) and superconductivity ($T_C < 46\text{K}$). In comparison with the XANES spectroscopy of the reference samples: Sr_2RuO_4 by Ru^{4+} and $\text{Sr}_2\text{GdRuO}_6$ by Ru^{5+} , a mixed-valence feature of Ru in these Ru-1212 compounds was found. That is, a combination of 0.4-0.5 Ru^{4+} and 0.6-0.5 Ru^{5+} valences.

Spin-crossover Phenomena of Encapsulated Transition Metal Complexes (Y. Wang, NTU)

The thermally driven spin transition of Co-containing complex $[\text{Co}(\text{bpy})_3][\text{LiCr}(\text{ox})_3]$ was observed on the near-edge structure of Co K-edge at 50-250 K. The spin transition is attributed to cobalt high spin ($t_{2g}^5 e_g^2$) to low spin ($t_{2g}^6 e_g^1$).

Electronic Structure of PtGa_2 (L. S. Hsu, NCHU; G. Y. Guo, NTU)

The electronic structure of PtGa_2 was studied using Pt L_3 -edge XANES. First-principle calculations based on density functional theory have been carried out to obtain the projected density of states. The Pt 5d projected density of states of PtGa_2 and pure Pt, and the Ga 3p projected density of states of PtGa_2 , are shown in Figure 8 to compare with the XANES data.

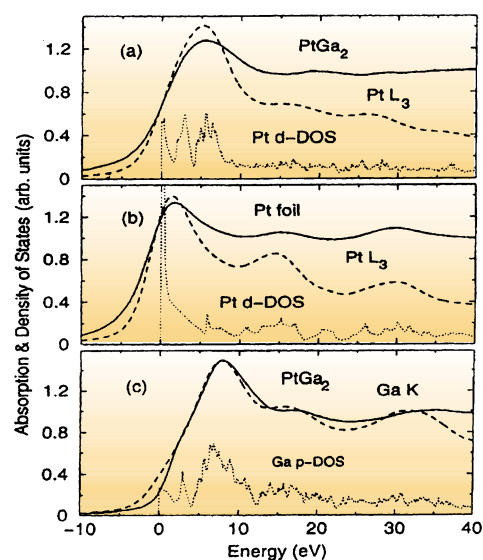


Figure 8 The experimental and theoretical Pt L_3 -edge XANES spectra for PtGa_2 and for Pt foil

In-situ XAS Investigation of $\text{LiAl}_{0.15}\text{Mn}_{1.85}\text{O}_4$ Cathode Materials (B. J. Hwang, NTUST)

Lithium manganese oxides are the most promising candidates for innovative lithium-ion batteries in terms of specific energy, non-toxicity, and low cost. Al dopants were used to substitute Mn^{3+} sites in LiMn_2O_4 spinel structure in order to avoid the Jahn-Teller distortion and hence capacity fading of this electrode material. Under cyclic voltammogram study, it was found that the valence of Mn is between 3.0 and 4.0 at open circuit potential. Fourier transformed EXAFS function showed that intensities of the first shell Mn-O and the second shell Mn-M ($M=\text{Mn}$ or Al) both increase with the cell potential, implying a lower degree of disordering as lithium ion is extracted from Li-Al-Mn-O materials.

Nano-structured Pt Clusters in MCM-41 (K. J. Chao, NTHU)

MCM-41 have hexagonal packed cylindrical pore channels with pore diameters in the range of 2 to 20 nm. In-situ XAS was used to probe the Pt clusters supported inside the pores under redox reactions. EXAFS of the

reduced samples showed that Pt particle size is 8 nm and 20 nm for 1 wt% and 10 wt% Pt/Al MCM-41, respectively.

Nanocrystalline FeS by Mechanical Alloying
(C. K. Lin, FCU; H. M. Lin, TTU)

The formation of FeS by mechanical mixing of elemental iron and sulfur was studied by EXAFS of Fe K-edge and XANES of S K-edge. The results showed that Fe_{1-x}S formed after 3h of milling and nanocrystalline Fe₅₀S₅₀ powders were successfully prepared after 15h of milling. (Figure 9)

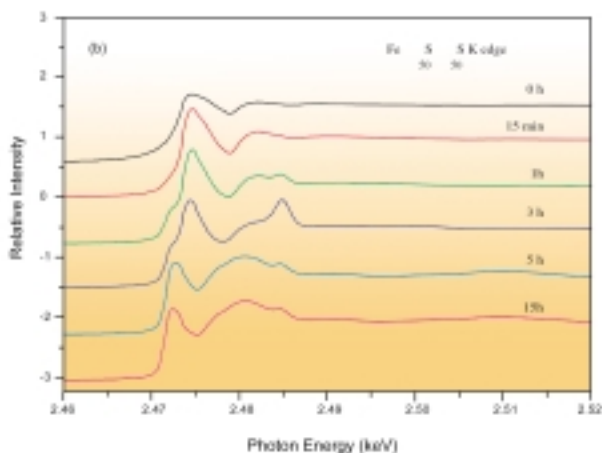


Figure 9 XANES of S K edge for Fe₅₀S₅₀ with different milling times.

Tricopper Clusters in the Particulate Methane Mono-oxygenase from Methanotrophic Bacteria
(S. I. Chan, Academia Sinica)

Particulate methane monooxygenase (pMMO) is a membrane-bound biochemical machinery (enzyme) that all methanotrophic bacteria can produce and utilize for the initial oxidation of methane to methanol. The X-ray absorption measurements have confirmed the classification of the 15 copper ions into 3 trinuclear copper clusters for electron transfer (E-clusters) and 2 trinuclear copper clusters for dioxygen chemistry and alkane hydroxylation (C-clusters). Systemetic studies of the reoxidation of the reduced protein with dioxygen and re-reduction of the pMMO by sodium dithionite revealed that only 30% of the copper contents can react

with dioxygen and be oxidized to Cu(II). The remaining reduced Cu(I) is much more stable in the air which would supply as an electron pool.

Blackfoot Disease: Arsenic in Well Water
(H. P. Wang, NCKU)

Arsenic speciation in the well water in the blackfoot disease endemic area in Taiwan is studied. Mainly As(V) was found. EXAFS shows As atoms have 4.3 nearest oxygen at 1.72 Å. Remediation of the As-contaminated soil by an electrokinetic process did not lead to any significant change.

(b) X-ray Diffraction and Scattering

Anomalous Dispersion Behavior of Multiple-Wave X-ray Diffraction at Resonance
(Y. P. Stetsko and S. L. Chang, NTHU)

A resonance perturbation Bethe (RPB) approach is newly developed to account for the observed anomalous behavior and to provide fundamental understanding of X-ray multiple-wave interaction at resonance. The proposed experimental and theoretical approaches allow for the determination of the changes of X-ray reflection phases under resonance conditions with a high accuracy. This provides a highly sensitive way for experimental investigation of the spectral distribution of reflection phase change due to the resonance. (Figure 10)

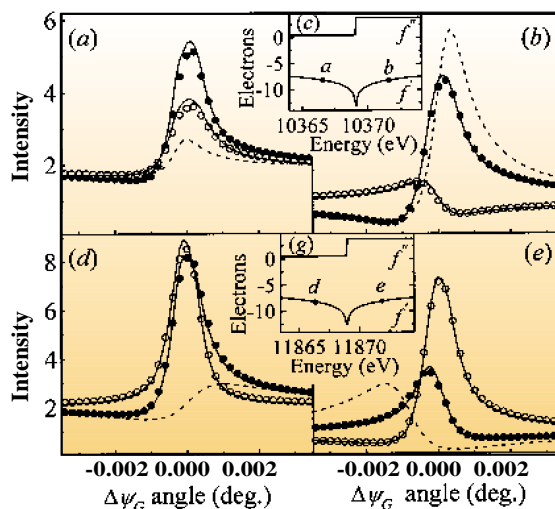


Figure 10 Calculated peak profiles at Ga (a, b) As(d, e) K-edge.

Evolution of Growth Mode in GaN:Mg Films (H.-H. Hung, SRRC)

GaN:Mg epitaxial films grown using MOVPE were studied. Magnesium can reduce the stacking fault energy difference between wurtzite and zinc-blende structures so as to make coexistence of two phases. In the heavily Mg-doped case, the surface-normal fiber-textured (10 $\bar{1}1$) structure is mediated with the screw dislocations, which are generated by prismatic step fronts with preferred (10 $\bar{1}1$) orientation of 8.4°-tilt but extending along the in-plane axial direction. According to DAFS results, apparent tensile strain and interstitial Mg are observed in these orientation-tilted structures. (Figure 11)

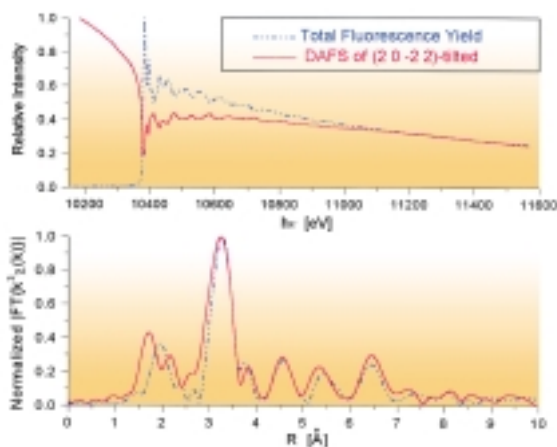


Figure 11 DAFS study of GaN(2 0 -2 2)-tilted phase: evidence of the interstitial Mg in tilted GaN wurtzite phase.

Magnetic Anisotropy of Epitaxy FePt on MgO (C.-H. Lee, NTHU; J. C. A. Huang, NCKU)

The strength of perpendicular magnetic anisotropy in FePt alloy films is strongly correlated with the long-range order parameter of the alloys. The order parameters of the FePt_x with $x = 0.8 \sim 1.5$ were measured with X-ray diffraction. Both the measured order parameters and the squareness of the magnetic hysteresis curves are found to correlate with the growth temperature of the films.

Pressure-induced Phase Transitions in Cd_{1-x}Fe_xSe (C. M. Lin, NHCT)

CdSe of wurtzite structure exhibits a pressure-induced phase transition to NaCl structure at 2.7 GPa. We measured this transition in Cd_{1-x}Fe_xSe with $x = 0.03, 0.05, 0.13, \text{ and } 0.16$. The transition was found at 3.0, 3.1, 3.4 and 3.7 GPa for these samples, respectively. (Figure 12)

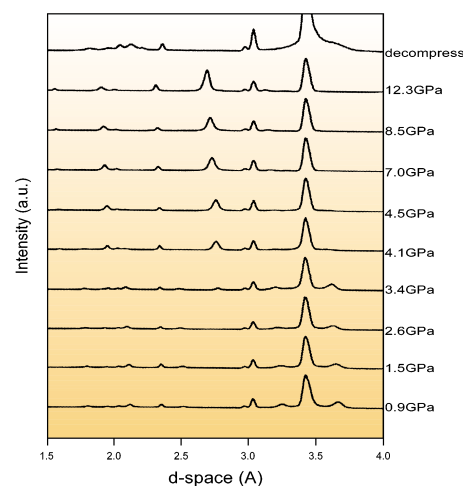


Figure 12 A series spectra of bulk Cd_{0.87}Fe_{0.13}Se at various pressure recorded in a loading run and process of decompression to ambient pressure.

In-situ XRD Study of Li-battery Cathode Materials (B. J. Hwang, NTUST; H. S. Sheu, SRRC)

Two kinds of secondary Li-battery cathode materials LiMn₂O₄ and Al-doped LiMn₂O₄ were investigated by in-situ XRD during charging and discharging both in aqueous solution and in EC + DEC(1:1) + LiPF₆ organic electrolyte. In aqueous solution a phase transition was found at the potential of 1.113 V in the charging process, while discharging the phase transition shift to 0.897 V. The charge/discharge cycling processes of Li-ion cell operated in organic electrolyte was investigated in the potential range of 3.3 to 4.3 V. The phase transition was found only in LiMn₂O₄ but not in the Al-doped system during cycling process. The Al-

doped electrode can therefore be a stable electrode for battery application. (Figure 13)

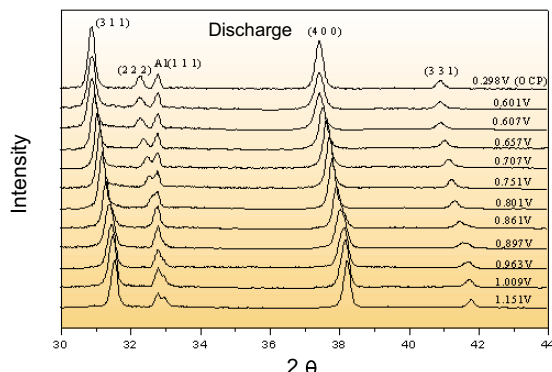


Figure 13 In-situ XRD patterns of $\text{LiAl}_{0.15}\text{Mn}_{1.85}\text{O}_4$ during charging process.

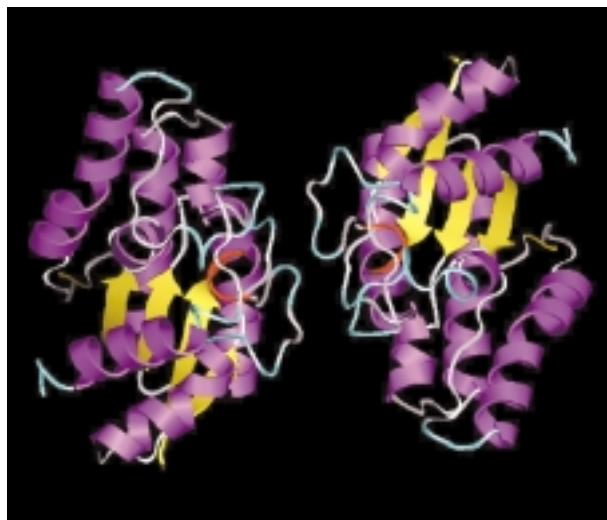


Figure 14 The 3D structure of Arylesterase.

Fracture Toughness of $\text{ZrO}_2(3Y)$ Ceramics by YNbO_4 Addition
(C.-C. Chou, NTU; H.-Y. Lee, SRRC)

The fracture toughness of $\text{ZrO}_2(3Y)$ specimens can be greatly enhanced by addition of YNbO_4 . In-situ compression high resolution diffraction experiments show that an unidentified stress-induced transformation occurs. Analyses of the stress-strain characteristics and the diffraction results suggest that fracture toughness of the specimens cannot be attributed to a tetragonal-to-monoclinic martensitic transformation.

(c) Protein X-ray Crystallography

High Resolution Structure Determination of Arylesterase from *Vibrio Mimicus*
(Y. C. Liaw, Academia Sinica; Y. C. Jean, SRRC)

The crystal structure of arylesterase from *Vibrio Mimicus*, which catalyzes the hydrolysis of ester bond with aromatic substrate preference, was solved by MAD method from Au derivative and refined up to 1.9Å resolution. The tertiary fold of the enzyme is different from the α/β hydrolase fold found in most of neutral lipases and esterases and is similar to small GTPase. (Figure 14)

Development of Microstructure Fabrication

High Performance Flat Miniature Heat Pipes Fabricated by UD-LIGA Process
(P. H. Chen, NTU; Y. Cheng, SRRC)

The high performance flat miniature heat pipe (FMHP) was successfully fabricated by ultra-deep LIGA (UD-LIGA) process developed at SRRC. The dimensions of microgrooves on the FMHP are 1 mm in depth, 100 μm in width, and 60 mm in length. The theoretically predicted results show that the dissipated heat flux can reach to 391 W at a working temperature of 100°C. (Figure 15)

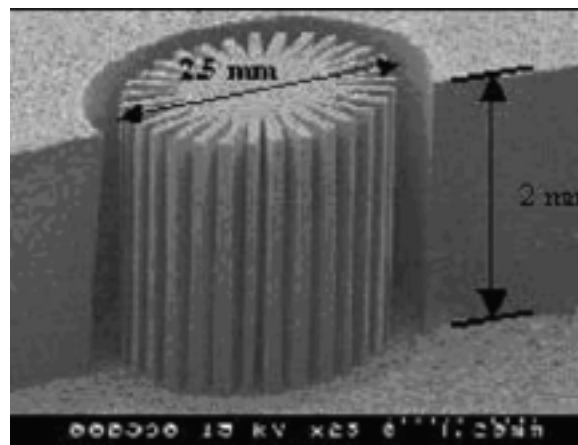


Figure 15 The PMMA microgrooves structures of the miniature heat pipe.

Thick-film Lithography using Laser Write (Y. Cheng, SRRC)

Mask-making process by laser direct-write has been broadly applied in the microelectronics and the PC board industries. The thick-film lithography of laser write was developed mainly for the X-ray mask in the LIGA application. Several schemes of multiple writing were successfully demonstrated in terms of the sidewall straightness and free from intensity fluctuation of laser light. Present study adopts the applications of positive resist of AZ P4620 prepared with a thickness of 30 μm , anti-reflection coating of AZ BARLi II on the substrate, and intensity filler to achieve smooth and straight sidewalls.

Nanometer Scale X-ray Mask Fabrication with Scanning Probe Lithography (J. T. Sheu, SRRC)

In addition to electron beam lithography and X-ray lithography (XRL), scanning probe techniques such as scanning near-field optical microscopy and scanning tunneling microscopy have been demonstrated for sub-50 nm nano-lithography. Using scanning probe lithography (SPL) technique, nanometer scale X-ray mask was fabricated so that nanometer structure or devices can be duplicated via XRL for diverse applications in nanotechnology. (Figure 16)

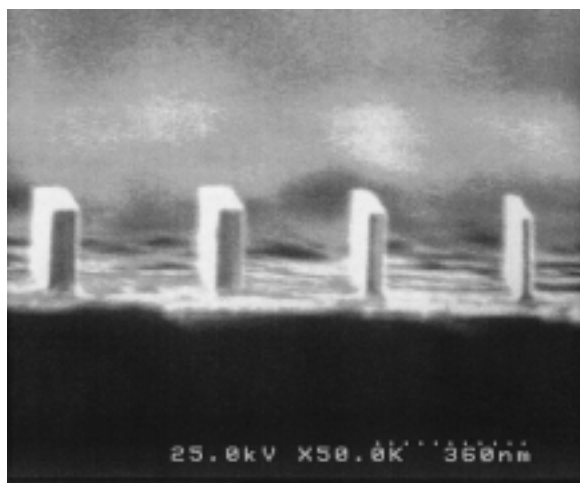


Figure 16 Silicon nanostructures fabricated by SPL and aqueous wet.